CrossMark

ORIGINAL ARTICLE

An experimental study on abrasive waterjet cutting of CFRP/Ti6Al4V stacks for drilling operations

A. Alberdi[1] · T. Artaza[1] · A. Suárez[1] · A. Rivero[1] · F. Girot[2]

Abstract In the present study, CFRP/Ti6Al4V stacks were machined with abrasive water jet using different process parameters in order evaluate the viability of AWJ industrial application as a substitute of conventional drilling. The effect of the stack configuration, the traverse feed rate, the cutting tool (combination of orifice and focusing tube diameter and abrasive mass flow rate), and the pressure over the kerf profile, taper angle, and surface roughness has been analyzed through an ANOVA analysis and related to the physical parameters of the AWJ process. As a result, a positive taper angle is observed in Ti6Al4V while a negative is observed in CFRP in almost all cutting conditions. This leads to obtain an X-type or barrel-type kerf profile depending on the stack configuration. In addition, the surface roughness can be as low as 6.5 μm in both CFRP and Ti6Al4V materials at 95 mm/min when CFRP/Ti6Al4V configuration is used.

Keywords AWJ · Drilling · Stacks · CFRP · Ti6Al4V · Waterjet

1 Introduction

One of the most important requirements within the aeronautical industry is to obtain lightweight structures to reduce carbon dioxide emissions and fuel consumption. High strength-to-density ratio materials, such as carbon fiber reinforced plastics (CFRP), titanium alloys (Ti6Al4V), and their joints known as CFRP/Ti6Al4V stacks are extensively used in this industry in order to fulfill this requirement. The conventional joining method is based on riveting technology, which includes a drilling step for producing the hole where the rivet is introduced.

Although the difference between the mechanical properties of Ti6Al4V and CFRP is desired for enhancing the strength and the lifetime of the aircraft components, it also supposes a big challenge for achieving the high quality of the hole demanded in the drilling process by the aeronautic sector. When drilling CFRP material, many different defects can be produced, such as fiber pullout, fiber break-out, and/or delamination, which may cause the rejection of the pieces. In fact, in the aeronautical field, the percentage of pieces rejected because of delamination ascends to 60 % [1]. Furthermore, CFRP is a highly abrasive material and depending on the fiber orientation, it can cause a severe tool wear, which is accelerated when using high cutting speeds [2–4]. Different drill designs and coatings are commonly employed for avoiding the tool wear [1, 5]. On the other hand, the low thermal conductivity of Ti6Al4V, its strong chemical affinity, and the chip welding to the cutting edge may lead to a premature tool failure. Moreover, the burr formation is also a troublesome in aerospace applications [6].

All the aforementioned problems turn CFRP/Ti6Al4V stacks drilling operations into a difficult task as far as each material needs very different cutting conditions. Actually, many drills and reamers are often used in the drilling process of one hole to obtain the required surface finish and tolerances. Moreover, a huge amount of holes are machined on these components, e.g., more than 250 holes are drilled in a central wing box. This makes the drilling process very expensive in terms of costs and productivity. Therefore, any progress or

✉ A. Alberdi
  amaia.alberdi@tecnalia.com

[1] Tecnalia Research and Innovation, Paseo Mikeletegi 7, 20009 Donostia-San Sebastián, Spain

[2] Ikerbasque, Basque Science Foundation - Department of Mechanical Engineering, Faculty of Engineering of Bilbao, University of the Basque Country, Alameda de Urquijo s/n, 48013 Bilbao, Spain

improvement of the drilling operation could significantly reduce the operation costs.

The study of AWJ technology as an alternative for stack drilling is worthwhile, since it has a lot of advantages in comparison with other techniques, e.g., its high machining versatility and flexibility, its capability to cut a wide range of materials and thicknesses, the absence of thermal damage, low tool wear, and low cutting forces. Other nonconventional technologies such as electrical discharge machining (EDM) and laser machining (LM) are not an effective solution to drill Ti6Al4V, due to the remaining large heat-affected zone and the limited surface quality [7, 8].

The AWJ drilling process consisted on two different steps: the piercing and the cutting step. First, during the piercing step (Fig. 1a), the jet impinges over the material in one position until the jet goes thought the material thickness. After that, during the cutting step (Fig. 1b), the jet moves over a circular path cutting the material until a hole with a desired diameter is obtained.

Despite the small amount of articles studying the drilling process by AWJ technology [9, 10] and the machining of hybrid titanium/graphite composite laminates [11], it is possible to find several references which have done the characterization of Ti6Al4V and CFRP materials separately [12–19]. Escobar-Palafox et al. [9] and Hussein Mohammed Ali Ibraheem et al. [10] developed mathematical models for predicting the quality of the hole as a function of process parameters based on statistical analysis. Pahuja et al. [11] studied the machining of hybrid titanium/graphite composite laminates by AWJ and found that surface roughness is higher

Fig. 1 AWJ drilling process: a piercing step; b cutting step
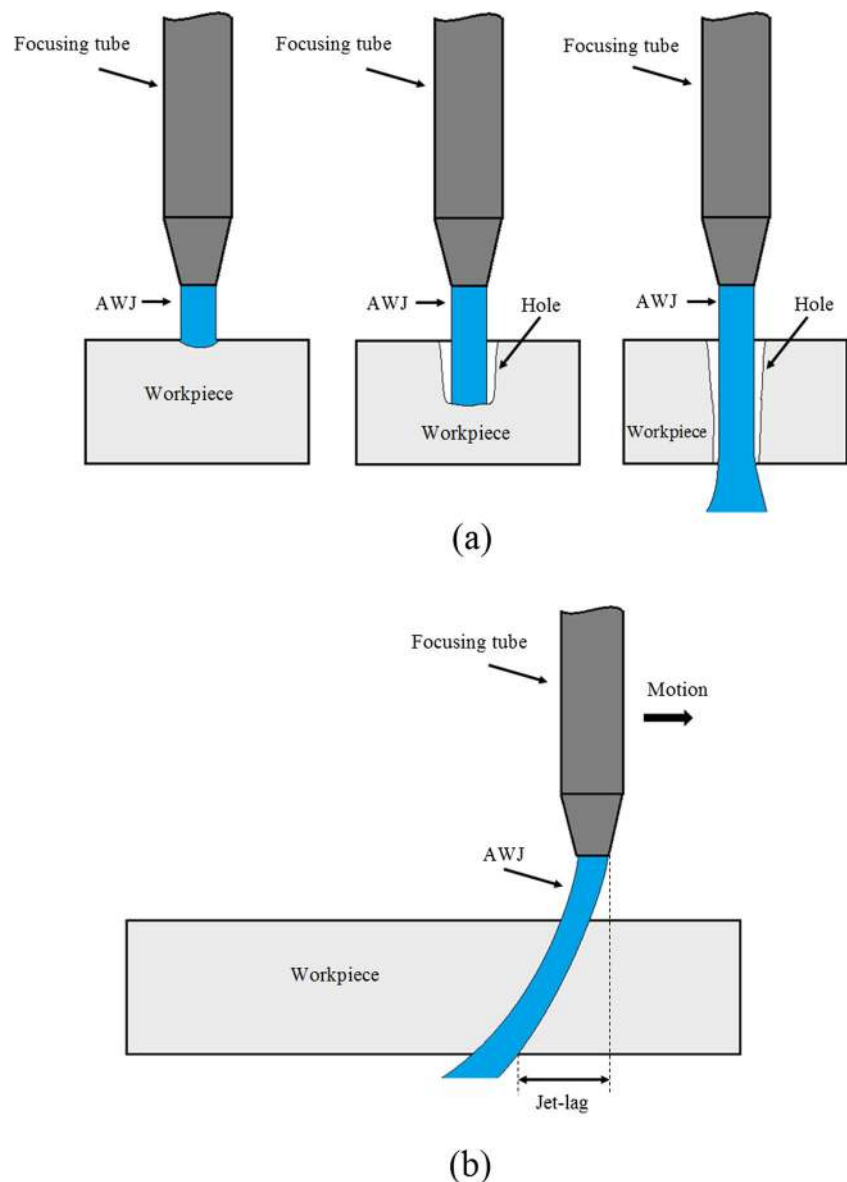
for small arc tool paths than for large arcs or straight cuts. In addition, they found different material removal mechanisms for different material phases and obtained similar conclusions as Seo et al. [12] and Arola and Ramulu [13, 14]: the titanium is cut by ductile shearing, abrasive ploughing, and scratching action; the matrix material is cut by shearing and plastic deformation; and the fibers are cut by microchipping, brittle fracture, and bending failure. Arola and Ramulu also found deformation and subsurface hardening in the AWJ machining of Ti6Al4V [15] and found three cutting regions including initial damage region (IDR), smooth cutting region (SCR), and rough cutting region (RCR) in both graphite/epoxy composites [13, 14] and Ti6Al4V [15].

Regarding the works studying the titanium and composite materials separately, Alberdi et al. [16] obtained the machinability of two different CFRPs and discussed the quality of the cuts in terms of the roughness and taper angle, which are dependent on the traverse feed rate and the material thickness. Regarding the taper angle, the results were always below 3.5°. Ramulu and Arola [17] have also considered how cutting feed direction with respect to the fiber orientation can affect to the surface roughness. The results show a difference of approximately 2 μm between the 90° cutting orientation (2.5 μm) and the 45° one (4.1 μm). Boud et al. [18] and Hascalik et al. [19] analyzed the influence of the traverse feed rate and abrasive type when cutting Ti6Al4V with AWJ technology. Regarding the abrasive characteristics, the geometry and material of the abrasive grains affect the material removal rate and the surface quality [14]. On the other hand, the results of several tests performed by Hascalik et al. [19] reveal that the traverse feed rate is a significant factor on the surface morphology, and that the widths and features of different regions formed in the cutting surface change according to this parameter. It was also observed that the kerf taper angle and surface roughness increase with increasing traverse feed rate.

In spite of the many advantages of AWJ technology in comparison with other technologies, its application to the AWJ drilling of CFRP/Ti6Al4V stacks has many drawbacks. The delamination of the CFRP that arises during the piercing process is one of the most important. This problem is a consequence of the impact from which the material suffers during the very first instants, when the jet is only consisted of water and the abrasive particles have not entered the mixing chamber yet [20]. However, there exist commercial solutions that avoid such type of problem.

This research work aims to study the influence of the AWJ process parameters on the surface quality (roughness and kerf profile) of the CFRP/Ti6Al4V stacks in the cutting step of the AWJ drilling process, in order to evaluate the viability of AWJ industrial application as a substitute of conventional drilling. The analyzed process variables are the pressure, the traverse feed rate, the stack configuration and the combination of abrasive mass flow rate, and the orifice and focusing tube diameter

(Fig. 2). In addition, a theoretical review of the physics of waterjet cutting process is performed, where three different parameters are obtained for analyzing the results obtained in the experimental part.

2 Physics of waterjet cutting

The physical understanding of the quality of the AWJ cutting materials indicates that the cut characteristics such as taper angle, roughness, and delamination mechanisms are a direct result of jet kinetic energy rate (dKE/dt), jet-work interaction time, and ratio of the jet velocity at the workpiece upper surface to the velocity at the piece lower surface [21–25].

Different experimental investigations of liquid jets penetrating into a quiescent fluid (Fig. 3) pointed out that the envelope containing the turbulence caused by the jet adopts a nearly conical shape. The diameter D of the jet is proportional to the distance x downstream from the nozzle location. It has also been demonstrated that the opening angle is near the same, independently of the nature of the fluid (air or water) and of other considerations (such as nozzle diameter and jet velocity). This universal angle is approximately 24°. It follows that the coefficient of proportionality between the jet diameter D and the downstream distance x from the nozzle exit is

$$D(x) = 2x\tan(12°) \approx 2x/5 \qquad (1)$$

Since the initial jet diameter is not zero but nozzle exit diameter d_e, the distance x must be counted not from the orifice but from a point of origin called the virtual source at a distance $5d_e/2$ into the focusing tube (Fig. 3).
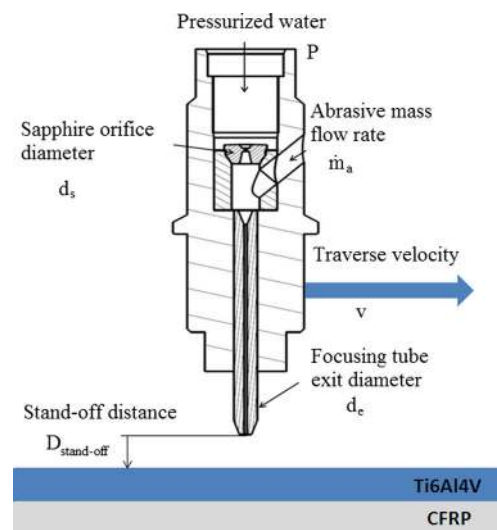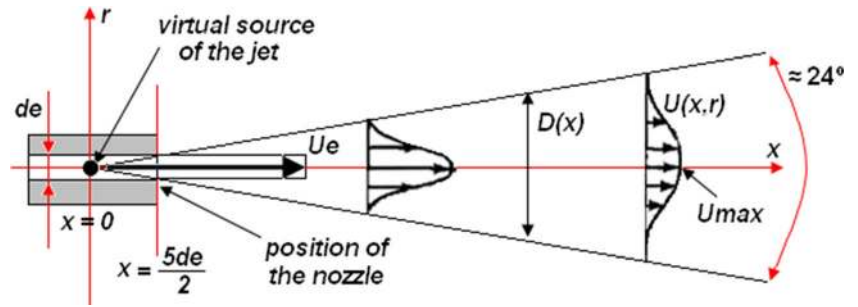

Fig. 2 AWJ process parameters

Fig. 3 Schematic description of a jet penetrating in a quiescent fluid

Many authors reported that the velocity in the jet obeys a law of similarity [21–25]. All cross sections appear identical, except for a stretching factor, and the velocity profile across the jet can be defined by a Gaussian function, as follows:

$$U(x,r) = U_{max} \cdot exp\left(-\frac{r^2}{2\sigma^2}\right) \quad (2)$$

where x is the downstream distance along the jet from the virtual source, r is the cross-jet radial distance from its centerline, $U_{max}(x)$ is the maximum speed at the centerline, and $\sigma(x)$ is the standard deviation related to the Gaussian profile of velocity. From statistics, it is known that the width of the distribution that encompasses 95 % of the area under the curve is equal to 4σ leading to

$$4\sigma = d_e \quad or \quad \sigma = x/10$$

and

$$U(x,r) = U_{max} \cdot exp\left(-\frac{50r^2}{x^2}\right) \quad (3)$$

When a jet enters a fluid at rest, the absence of external accelerating or decelerating forces implies that the momentum flux in the jet's cross section remains constant downstream. The total flux of x-momentum, integrated on r at any position x, is a constant, independent of x:

$$\int_0^\infty \rho U(x,r)^2 2\pi r dr = \rho U_e^2 \frac{\pi d_e}{4} \quad (4)$$

where U_e and d_e are, respectively, the average exit velocity and the nozzle exit diameter. Substituting Eq. 3 into Eq. 4 and after integration, one can deduce that

$$U_{max} = \frac{5d_e}{x} U_e \quad (5)$$

The velocity along the centerline of the jet decreases inversely with the distance from the virtual source. The average velocity associated to this maximum velocity is defined as follows:

$$\overline{U}(x) = \frac{4}{\pi D(x)^2} \int_0^\infty U(x,r) 2\pi r dr = \frac{U_{max}}{2} = \frac{5d_e}{2x} U_e \quad (6)$$

The jet kinetic energy rate at the piece upper surface is given by

$$\frac{dKE}{dt} = \frac{1}{2} \dot{m}_a \overline{U}\left(\frac{5d_e}{2} + D_{stand-off}\right) \quad (7)$$

where $\dot{m}_a$ is the abrasive mass flow rate and $\overline{U}(x)$ is the AWJ average velocity at the upper surface of the CFRP part, assuming that the particle has gained the same velocity as its surrounding water at the point of particle impingement on the target material.

The AWJ velocity $\overline{U}_e$, after mixing with abrasives, can be determined using the momentum transfer equation:

$$\overline{U}_e = \psi\left(\frac{\dot{m}_w}{\dot{m}_s}\right) U_w \quad (8)$$

where ψ is the momentum transfer efficiency, $\dot{m}_w$ is the water mass flow rate from the orifice, and $\dot{m}_s$ is the slurry mass flow rate including the water mass flow rate and the added abrasive mass flow rate.

The momentum transfer efficiency is defined as follows:

$$\psi = \sqrt{\frac{P_0}{P(1-n)}\left[\left(1+\frac{P}{P_0}\right)^{1-n}\right]-1} \quad (9)$$

where $P_0 = 300$ MPa and $n = 0.1368$ at 25 °C.

The waterjet velocity U_w from the orifice may be found by applying the Bernoulli's equation:

$$U_w = \chi\sqrt{\frac{2P}{\rho_w}} \quad (10)$$

where P is the water pressure, ρ_w is the water density, and χ is the discharge coefficient that accounts the momentum losses due to wall friction, fluid-flow disturbances, and the compressibility of the water.

According to Chen et al. [26], the discharge coefficient varies linearly from 0.85 to 0.90 with the water pressure ranging from 90 to 350 MPa.

The water density depends also on the pressure as follows:

$$\rho_w = \rho_0 \cdot \left(1 + \frac{P}{P_0}\right)^n \tag{11}$$

with ρ_0=1134 kg/m^3 and P_0=300 MPa.

Substituting Eqs. 8 and 11 into Eq. 7 and taking into account that the mass ratio term may be approximated to a constant K_m [27] (in our case this factor varies between 0.87 and 0.92), we obtain

$$\frac{dKE}{dt} = \psi^2 \chi^2 K_m^2 \frac{25 d_e^2}{4 \rho_w} \frac{P \dot{m}_a}{\left(\frac{5 d_e}{2} + D_{stand-off}\right)^2} \tag{12}$$

The jet kinetic energy rate is then proportional to

$$\pi 1 = \frac{P \dot{m}_a}{\left(\frac{5}{2} + \frac{D_{stand-off}}{d_e}\right)^2} \tag{13}$$

When cutting stacks laminates, the cutting of the lower laminates depends on the energy loss of the jet when cutting the upper material. The energy rate necessary to cut the upper material can be evaluated as follows:

$$\frac{dE_{cutting}}{dt} = \sigma_{target\ mat} \cdot e_{target\ mat} \cdot V_t \cdot D(x) \tag{14}$$

with σ the cutting specific energy or the flow stress of the upper laminate material (target material), e the thickness of this laminate, and $D(x)$ the waterjet diameter at the surface of the upper material. Using Eq. 1, Eq. 14 reduces to

$$\frac{dE_{cutting}}{dt} = \frac{2}{5} \cdot \sigma_{target\ mat} \cdot e_{target\ mat} \cdot V_t \cdot \left(\frac{5 d_e}{2} + D_{stand\ off}\right) \tag{15}$$

In order to define the energy rate of the waterjet, it is necessary to determine the value of the K_m coefficient. K_m is defined as the mass ratio term:

$$K_m = \frac{\dot{m}_w}{\dot{m}_s} = \frac{\dot{m}_w}{\dot{m}_w + \dot{m}_a} \tag{16}$$

where $\dot{m}_w$ is the mass ratio of water, $\dot{m}_s$ is the mass ratio of the slurry, and $\dot{m}_a$ is the mass ratio of abrasive particles.

The water mass ratio can be defined as follows, using Eqs. 8 to 10:

$$\dot{m}_w = \rho_w \cdot \frac{\pi \cdot d_s^2}{4} \cdot \psi \cdot \sqrt{\frac{2P}{\rho_w}} = \frac{\pi \cdot d_s^2}{4}$$

$$\cdot \sqrt{\frac{2 \cdot P_0 \cdot \rho_0}{(1-n)} \cdot \left[\left(1 + \frac{P}{P_0}\right)^{1-n}\right] \cdot \left[1 + \frac{P}{P_0}\right]^n} \tag{17}$$

where d_s is the diameter of the sapphire orifice.

The energy loss ratio of the water jet after cutting the upper part can be defined as follows:

$$\pi 2 = \frac{dE_{cutting}/dt}{dKE/dt} \tag{18}$$

Thus, the total kinetic energy rate is proportional to

$$\pi 1 \cdot (1-\pi 2) = \frac{P \dot{m}_a}{\left(\frac{5}{2} + \frac{D_{stand-off}}{d_e}\right)^2} \cdot \left(1 - \frac{dE_{cutting}/dt}{dKE/dt}\right) \tag{19}$$

The values of specific energy of the target or upper materials used are given in Table 1.

The jet exposure time is then defined as follows:

$$t_{exposure} = \frac{d_e}{v} \tag{20}$$

where v is the velocity of the nozzle traverse and d_e the diameter of the focusing exit nozzle.

During the exposure time, the CFRP material is exposed to an abrasive power which allows defining an abrasive jet exposure parameter as follows:

$$\pi 3 = \frac{d_e \dot{m}_a}{v} \tag{21}$$

3 Experimental setup and methodology

The experimentation consisted on performing straight-cuts at different conditions. The length of each cut was 70 mm. The material used for experimental tests were two T800/924C CFRP plates (250×150×11 mm) and two Ti6Al4V plates (250×150×10 mm).The plates were tied by means of four bolted unions, and test piece was fastened to the machine with two jaws as it can be seen in Fig. 4.

Experiments were carried out on a Byjet L2030® machine, provided with a high-pressure pump ByPump 50APC®, which can reach a working pressure of 360 MPa.

As a result, the average roughness and the top and bottom kerf widths were measured. The taper angle was evaluated using the Eq. 22.

$$T = arctan\left(\frac{Wt - Wb}{2t}\right) \tag{22}$$

Table 1 Properties of the components of the metal/CFRP stacks

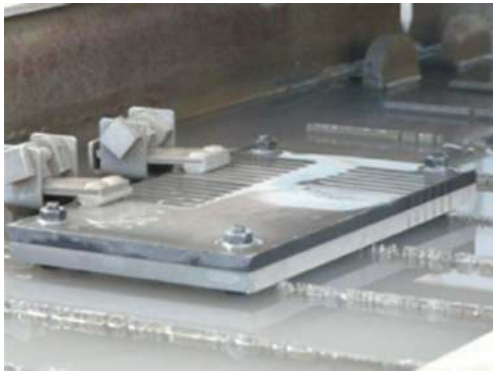| Component	Machinability	Specific energy
Ti6Al4V	82	1100 MPa
CFRP (T800/924C)	265	340 MPa

Fig. 4 Test piece setup and jaws

The roughness measurements were performed with a Mitutoyo SV-2000N2 roughness tester. The average mean surface roughness (R_a) of all tests was evaluated in a length of 15 mm using a Gaussian filter and a cutoff length of 2.5 mm. Roughness measurements were taken at 10 % of the thickness from the bottom edge, since in this region, the roughness reaches its maximum value (Fig. 5). The top and bottom kerf widths of the cuts were characterized with a stereoscopic-trinocular-microscope Motic® SMZ-143 Series with a range of magnification from 15× to 60×. The observed image has been captured with a Clemex© L 2.0 camera and has been analyzed by means of Clemex Captiva 5.0© software.

The design of experiments was based on a factorial design, which incorporated four factors: pressure (P), traverse speed (v), stack configuration, and cutting tool (defined as a combination of the orifice diameter, d_s, focusing tube exit diameter, d_e, and abrasive mass flow rate, $\dot{m}_a$). The selected levels for each factor are stated in Table 2. The selected ratios between the focusing tube exit diameter and the orifice diameter was close to 3 as generally suggested by many manufacturers [16]. Moreover, for each tool, an optimum value of abrasive mass flow rate was selected based on AWJ process models obtained by the authors [28]. The standoff distance was fixed at 2 mm and the abrasive used for the experimentation was a Garnet GMA #80. The combination of all factors and levels resulted in 56 different conditions.
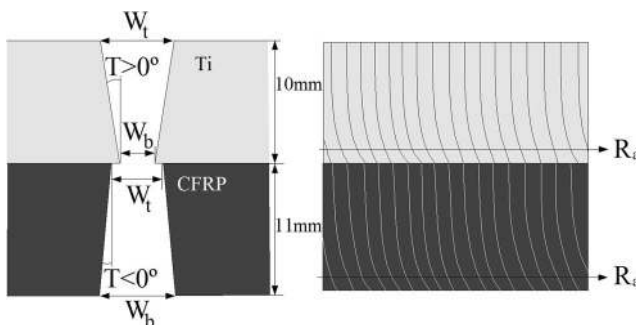

Fig. 5 Example of kerf profile and roughness measurements (Ti6Al4V/CFRP configuration)

Table 2 Process parameters and experimental levels

Process parameters	Levels
P (MPa)	250, 360
Stack configuration	Ti6Al4V/CFRP, CFRP/Ti6Al4V
$d_s/d_e/\dot{m}_a$ (mm-mm-g/min)	0.25/0.76/350 and 0.35/1.02/450
v (mm/min)	5, 20, 35, 50, 65, 80, 95

4 Results and discussion

The effect of the process parameters on the stack cutting was investigated through an analysis of variance (ANOVA). In fact, this is a computational technique conducted to learn about the influence of various design factors on the output. The results have been discussed in terms of taper angle, kerf widths (top and bottom), and surface roughness. To evaluate the effect of each studied factor in each output, the Fisher's test (or F test) was performed. The F value for each output compares the variance associated with that result with the residual variance. It is the mean square for the term divided by the mean square of the residual. Thus, large F values indicate that there is a big change on the output due to the variation of the analyzed factor. The p value indicates the probability to obtain the observed F value if the null hypothesis is true (there is no relationship between two measured phenomena), hence the probability to have an insignificant factor. In this analysis, factors whose p values resulted inferior to 10 % were considered significant. Table 3 shows the analysis concerning the taper angle and the roughness of Ti6Al4V and CFRP materials and the respective influence of the selected factors. Table 4 points out the Pearson correlation coefficient between the physical parameters as defined in Sect. 2 and the taper angle and roughness results. The resulting values of the physical parameters π1, π2, and π3 for each experimental test are given in the Appendix.

4.1 Analysis of the taper angle

According to the ANOVA analysis, the most significant factors for the taper angle on both materials are the pressure and the stack configuration (p value<0.0001). In addition, the traverse rate is also a significant factor because varying this parameter influences the taper angle can keep positive or negative values. Finally, while the cutting tool is significant for the taper angle obtained in Ti6Al4V, it is not a significant factor for the CFRP material. The graphics in Fig. 6 show how the influence of the pressure and the traverse feed rate on the taper angle in the two materials.

In Fig. 6, it can be observed that both in Ti6Al4V and CFRP the taper angle decreases when increasing the pressure due to the higher energy of the jet. The taper angle also decreases in Ti6Al4V when it is located in the upper part of the

Table 3 ANOVA analysis of taper angle and roughness

Factor	Taper angle Ti		Taper angle CFRP		Roughness Ti		Roughness CFRP	
	F value	p value	F value	p value	F value	p value	F value	p value
P	46.8909	<0.0001	67.4685	<0.0001	8.9994	0.0042	2.71063	0.1058
$d_s/d_e/m_a$	7.9596	0.0068	0.4082	0.5261	1.08880	0.3017	2.6293	0.1111
v	3.5258	0.0661	98.7131	<0.0001	474.1388	<0.0001	299.7120	<0.0001
Config	84.9501	<0.0001	1247.7147	<0.0001	15.6712	0.0002	236.3105	<0.0001
Residual error (sum of squares)	7.88		0.41		0.034		1.052×10^{-3}	

stack instead of the bottom part, because the jet also has higher energy. Nevertheless, the opposite is observed in CFRP material, i.e., the taper angle increased when it is located in the upper part of the stack. The results of the Pearson correlation coefficients (Table 4) also indicate the same trends. The correlation coefficient between the taper angle and the total energy parameter (Eq. 19) is negative for the Ti6Al4V, which means that the taper angle decreases when increasing the total energy of the jet. For the CFRP material, this correlation coefficient is positive. To understand the positive correlation between the taper angle of CFRP and the total energy of the jet, the effect of the stack configuration over the top and bottom width should be analyzed, since the taper angle is a result of the combination of the top and bottom widths as indicated in Eq. 22. In CFRP, the top and bottom kerf widths are increased when increasing the total energy of the jet in all configurations, as indicated their positive correlation coefficient (Table 4). In addition, in Fig. 7a, it can be observed that the top kerf width is higher for the CFRP when it is located on the upper part of the stack material (CFRP/Ti6Al4V configuration) than when it is located in the bottom part (Ti6Al4V/CFRP configuration) for the same cutting condition. On the other hand, Fig. 7b indicates that the bottom kerf width of the CFRP is not affected by the stack configuration. In addition, for the Ti6Al4V/CFRP configuration, the bottom kerf width is always higher than the top kerf width, so a negative taper angle is always obtained according to Eq. 22. Nevertheless, for the opposite configuration (CFRP/Ti6Al4V), the bottom kerf width is not always higher than the top kerf width, so a positive or negative taper angle can be obtained depending on the cutting condition. The combination of these results leads to a higher taper angle for the CFRP material when it is located in the upper part of the stack material, although the higher total jet energy.

Regarding the taper angle in Ti6Al4V, it is generally positive in both configurations. This occurs because the machinability index of the Ti6Al4V alloy is much lower than the machinability index of the CFRP material [16]. The machinability index is defined as a kinetic response of a workpiece material subjected to a certain machining operation and condition, which refers to the ease or difficulty with which this material can be machined [29]. Thus, the Ti6Al4V alloy needs higher energy to reach the zero taper point, defined as the traverse feed rate at which the taper angle passes from a negative value to a positive value for a certain material thickness and certain cutting conditions. For example, at 360 MPa of pressure with an orifice and focusing tube diameter of 0.25 and 0.76, respectively, and 350 g/min of abrasive mass flow rate, the zero-taper point is of 150 mm/min for the CFRP and of 12 mm/min for the Ti6Al4V.

Finally, the taper angle increases when increases the traverse feed rate as can be observed in Fig. 6. In Ti6Al4V, the Pearson correlation coefficient between the taper angle and the jet exposure parameter π3 is negative, which means that the taper angle increases when decreasing the jet exposure, so according to Eq. 21 when increasing traverse feed rate. In CFRP material, the correlation between the taper angle and the parameter π3 is very low. However, this coefficient is distorted by the effect of the stack configuration and the pressure, i.e., by the effect of the total energy parameter. Therefore, the correlation coefficient between the taper angle in CFRP and the jet exposure parameter π3 has been calculated for each stack configuration. As a result, the correlation coefficient descends to −0.8552 for CFRP/Ti6Al4V configuration, while it becomes almost zero for the Ti6Al4V/CFRP configuration. Thus, in the first configuration, the taper angle increases when

Table 4 Pearson correlation coefficient between outputs and physical parameters

Physical parameter	Ti6Al4V				CFRP			
	Taper	W_{top}	W_{bottom}	R_a	Taper	W_{top}	W_{bottom}	R_a
$\pi1 \cdot (1-\pi2)$	−0.6861	0.0898	0.5351	−0.5306	0.6739	0.8251	0.5612	−0.8167
π3	−0.7051	0.68103	0.8866	−0.5416	−0.2089	0.5851	0.8500	−0.3302

Fig. 6 Variation of taper angle as a function of pressure and traverse feed rate using an orifice and focusing tube diameter of 0.25 and 0.76 mm, respectively, and an abrasive mass flow rate of 350 g/min: **a** in Ti6Al4V (CFRP/Ti configuration); **b** in Ti6Al4V (Ti/CFRP configuration); **c** in CFRP (CFRP/Ti configuration); **d** in CFRP (Ti/CFRP configuration)
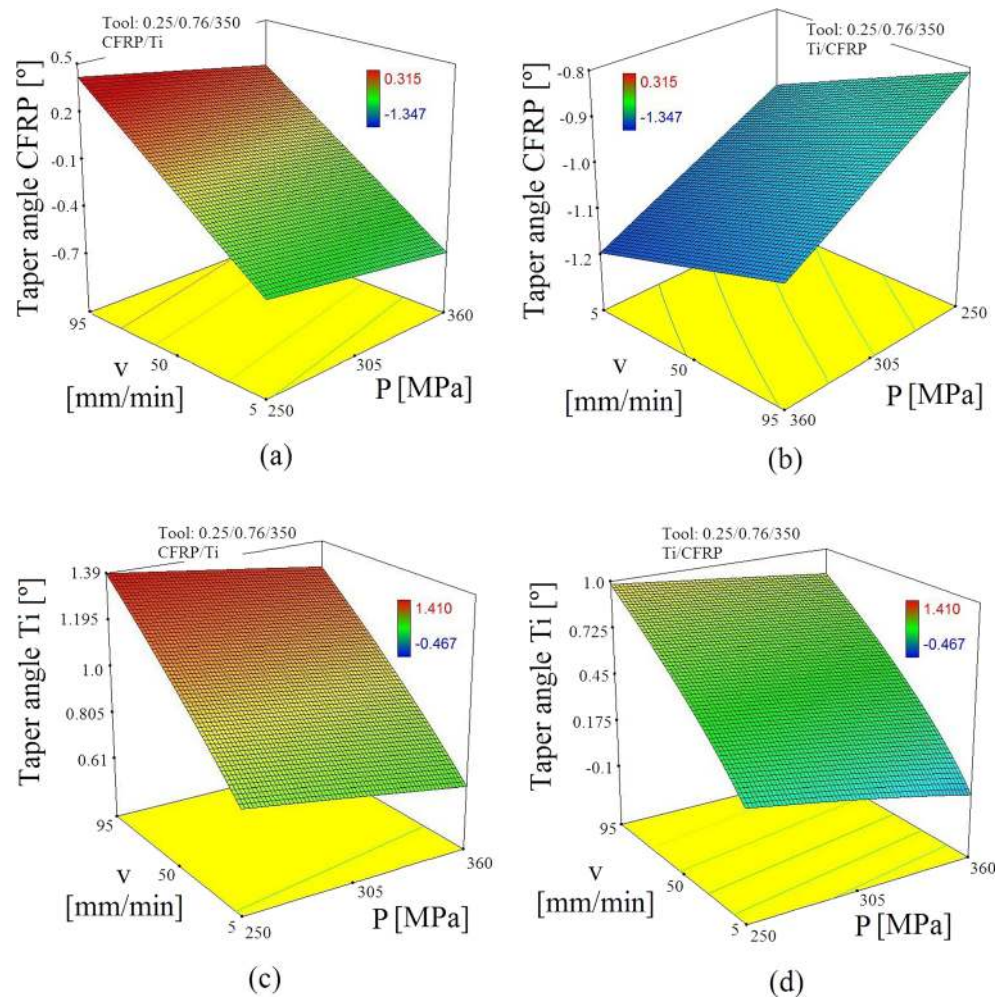
decreasing the jet exposure, but when the CFRP is located in the bottom part of the stack material, there is no correlation between the taper angle and the jet exposure. This occurs because the increasing rate of the top and bottom kerf width with the jet exposure is the same in the Ti6Al4V/CFRP configuration (Fig. 8a), while the increasing rate of the bottom kerf width is higher than in the top kerf width in CFRP/Ti6Al4V configuration (Fig. 8b).

4.2 Analysis of the kerf profile

The combination of the taper angles and the top and bottom widths of Ti6Al4V and CFRP materials results in a different kerf profile of the cuts, which depends mainly on the stack configuration. If Ti6Al4V is placed on top of the CFRP plate, the profile would acquire an X form, whereas if the contrary configuration is used, this form would be similar to a barrel
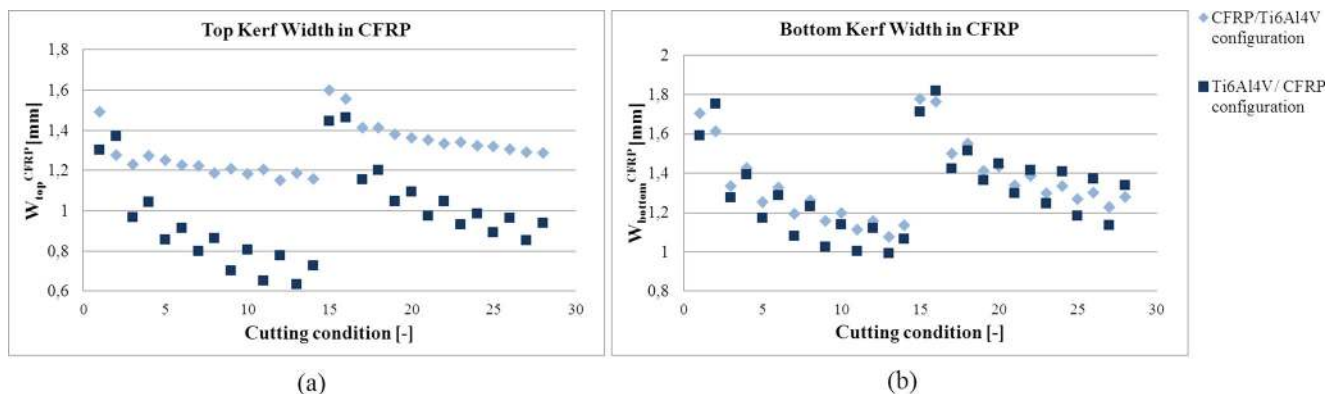

Fig. 7 Top and bottom kerf widths and taper angle in CFRP material for different configurations: **a** top kerf width; **b** bottom kerf width
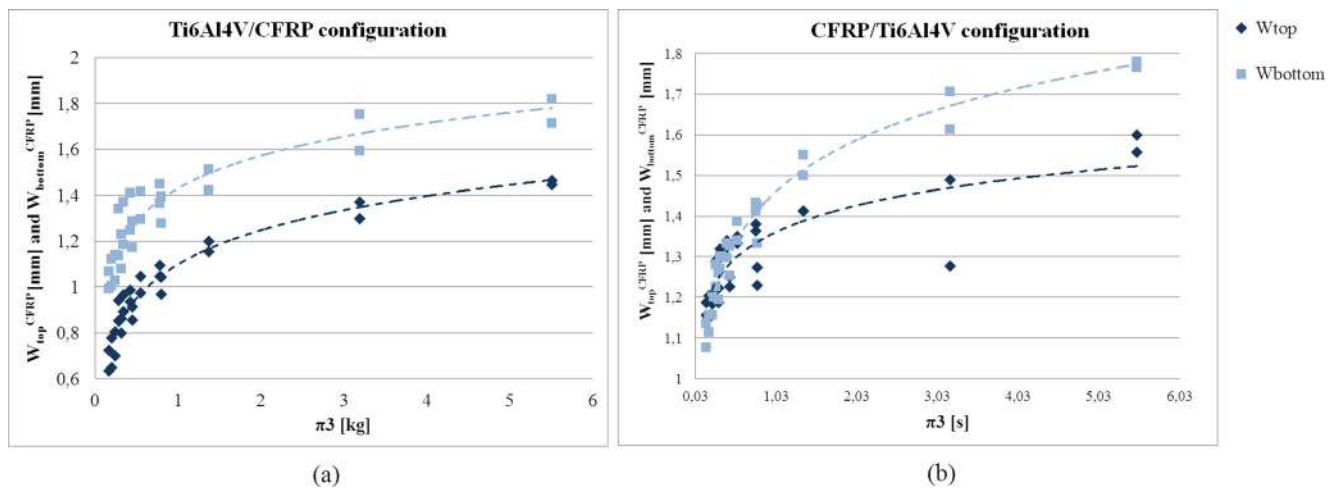
Fig. 8 Top and bottom kerf widths in CFRP material as a function of jet exposure parameter $\pi3$: **a** Ti6Al4V/CFRP configuration; **b** CFRP/Ti6Al4V configuration

(Fig. 9). This is because the taper angle of the Ti6Al4V is generally positive in both configurations, while the taper angle of the CFRP is negative in almost all conditions, as explained before. Figure 9 shows the evolution of the kerf profiles according to the traverse feed rate. Due to the differences obtained in the taper angle in CFRP and Ti6Al4V materials, the taper angle compensation using a five-axis machine [21] does not represent an effective solution for cutting CFRP/Ti6Al4V stacks, which consisted on tilting the head for compensating the taper angle for obtaining the zero taper point.

Top and bottom widths are also influenced by the type of tool, more concretely, by the combination of

the orifice and the focusing tube diameter and the abrasive mass flow rate. If the tool combination is 0.25/0.76/350 instead of 0.35/1.02/450, all widths become smaller, as far as the diameter of the focusing tube is smaller in the first case, the diameter of the jet is also smaller, thus decreasing the widths of the final cuts. In addition, if the pressure is equal to 360 MPa rather than 250 MPa, the jet gains an important amount of energy and the force of impact on the material also increases. This fact enables the jet to machine a higher amount of material. In fact, the only thing that varies after comparing the profile geometries at the same pressure value
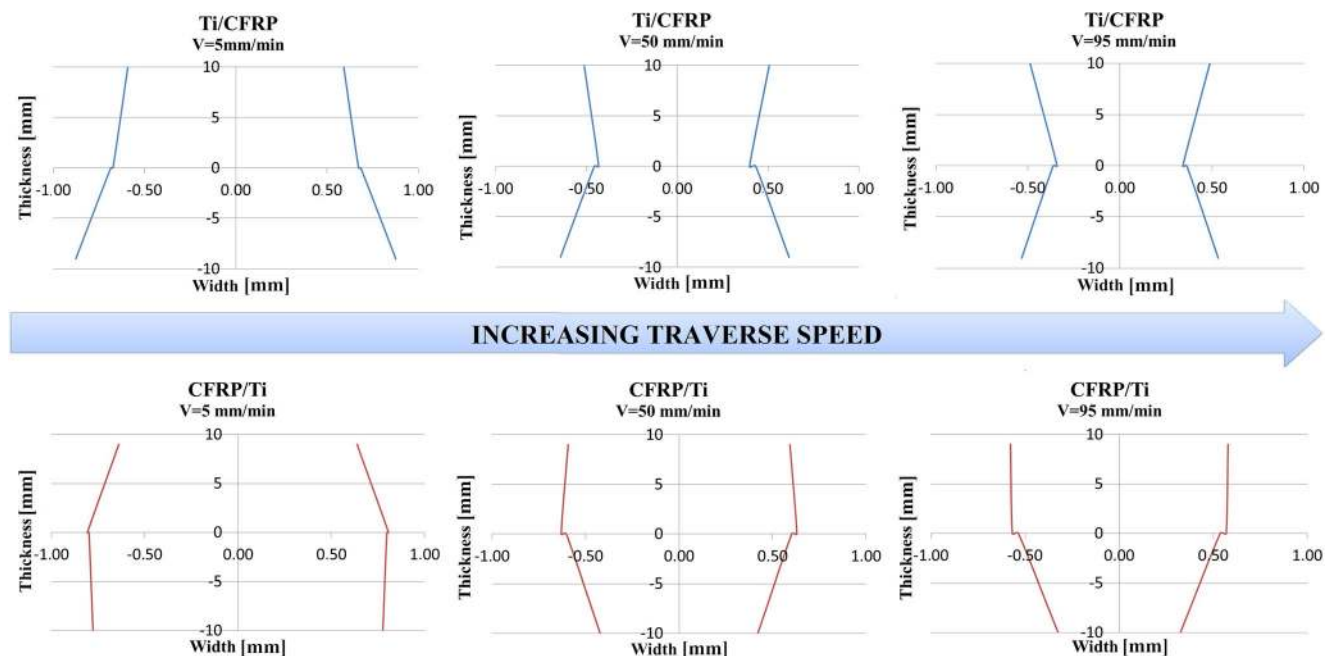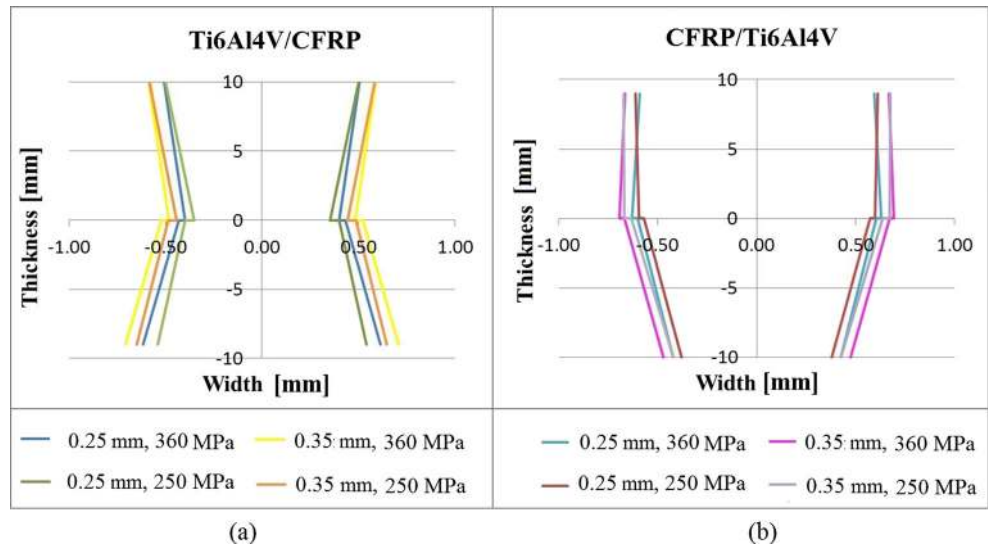

Fig. 9 Evolution of the kerf profiles as a function of traverse feed rate

(a)   (b)

but different tool sizes is the magnitude of the widths, as the lines defining these profiles are almost parallel (Fig. 10).

Another remarkable result that can be observed in Figs. 9 and 10 is the existing difference between the widths of the cuts on the different materials at the interface region. This phenomenon could be associated to the machinability characteristics of both materials: as the carbon fiber is an easier-to-cut material, the obtained width for this material is greater than the one for the Ti6Al4V using the same conditions. In fact, Ti6Al4V is a very hard material with a low machinability index. This width difference mitigates as long as lower values of traverse feed rate are used.

4.3 Analysis of the average surface roughness

According to the ANOVA analysis, similar conclusions can be obtained for the CFRP and Ti6Al4V materials. All factors are significant for the average roughness except the tool combination, i.e., the combination of the orifice and focusing tube diameter and abrasive mass flow rate. The most significant factor for the average roughness is the traverse feed rate, followed by the stack configuration and the pressure. In Fig. 11, the influence of these parameters can be observed for an orifice and focusing tube diameter of 0.25 and 0.76, respectively, and an abrasive mass flow rate of 350 g/min. The roughness increases exponentially as the traverse feed rate increases because the exposure time of the jet is lower, i.e., the correlation coefficient between the roughness results and $\pi 3$ coefficient is negative (Table 4). Regarding the stack configuration, when the material plate is located in the bottom part of the stack, the resulting average surface roughness is higher than when it is located in the upper part, because the energy of the jet impinging over the material is lower. When Ti6Al4V is placed over CFRP, Ti6Al4V roughness values range from 2.3

to 7.5 μm, while when it is placed below CFRP, roughness values for Ti6Al4V become a bit higher and vary from 3 to 10 μm. Regarding the CFRP material, when it is located over
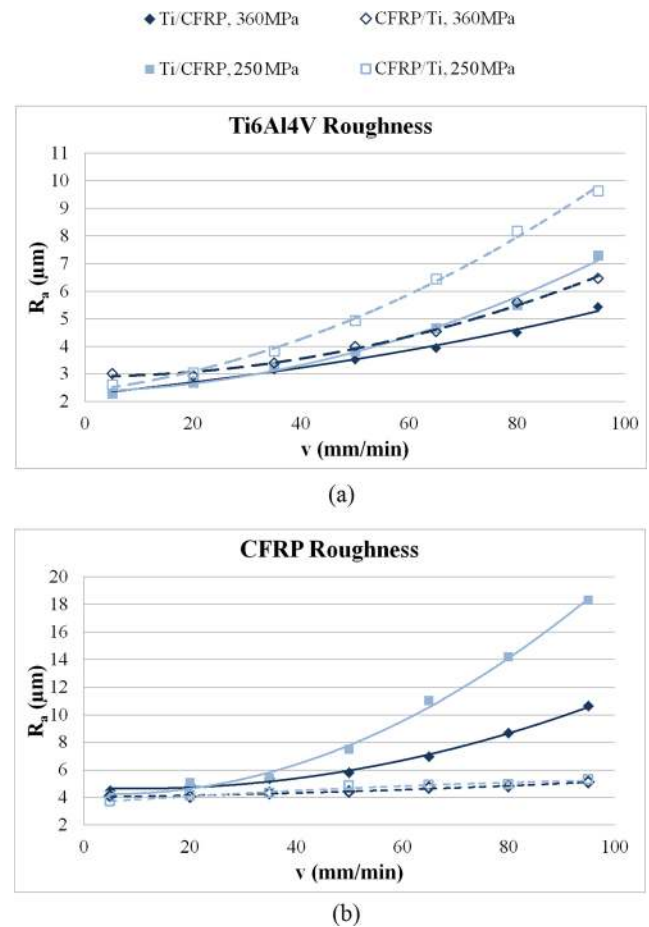

(a)

(b)

Fig. 11 Average roughness as a function of traverse feed rate for a orifice and focusing tube diameter of 0.25 and 0.76, respectively, and an abrasive mass flow rate of 350 g/min: **a** for the Ti6Al4V plate; **b** for the CFRP plate

the Ti6Al4V, the traverse feed rate has very little effect and the roughness values vary only from 4 to 5.5 μm. On the other hand, when it is located in the bottom part, the roughness values vary from 4 to 18 μm. Finally, when lower pressure is used, higher roughness values are obtained due to the lower energy of the jet. Similar trends have been observed when using the other tool combination (an orifice and focusing tube diameter of 0.35 and 1.02, respectively, and an abrasive mass flow rate of 450 g/min). The correlation coefficients also indicate that there is a negative correlation between the jet total energy (Eq. 19) and the average roughness (Table 4), which means that the roughness decreases when increasing the jet energy.

5 Conclusions and further lines

This work presents, for the first time, an analysis of the taper angle, the kerf profile and the average roughness for the cut of Ti6Al4V/CFRP stacks by means of abrasive waterjet technology. The combination Ti6Al4V and CFRP materials present a difficulty to machine using conventional approaches due to the dissimilar mechanical characteristics of them. The development of new techniques for machining stacks could help the aeronautic industry to enhance the manufacture and to better satisfy the increasing demand of this type of stack materials.

An ANOVA allows pointing out the effect of the AWJ process parameters on taper angle, kerf profile, and surface roughness, leading to the following conclusions:

– The most significant factors for the taper angle on both materials are the pressure and the stack configuration, followed by the traverse feed rate. The taper angle decreases when increasing the pressure due to the higher energy of the jet. The taper angle is lower in Ti6Al4V when it is located in the upper part of the stack than when it is located in the bottom part, because the jet also has higher energy. Nevertheless, the opposite is observed in CFRP material. This occurs due to the effect of the stack configuration on the top and bottom kerf widths. Finally, the taper angle increases when increases the traverse feed rate except in the CFRP material when it is located in the bottom part, because the increasing rate of the top and bottom kerf width with the jet exposure is the same in the Ti6Al4V/CFRP configuration.

– The taper angle of the Ti6Al4V is generally positive in both configurations, while the taper angle of the CFRP is negative because the machinability index of CFRP materials is much higher than the machinability index of the Ti6Al4V alloy. This also leads to a difference between the widths of the cuts on the different materials at the interface region.

– The choice of configuration, Ti6Al4V/CFRP or CFRP/Ti6Al4V, determines the profile geometry, which can respectively take the form of an "X" or be similar to a barrel's geometry.

– A taper angle compensation using a five-axis machine does not represent an effective solution in order to correct the profile's geometry, as the taper angle in Ti6Al4V and CFRP is completely different. The most significant factor for the average roughness is the traverse feed rate, followed by the stack configuration and the pressure. The roughness increases exponentially as the traverse feed rate increases because the exposure time of the jet is lower. When the material plate is located in the bottom part of the stack, the resulting average surface roughness is higher than when it is located in the upper part, because the total energy of the jet impinging over the material is lower. Finally, when lower pressure is used, higher roughness values are obtained due to the lower energy of the jet.

– When using CFRP/Ti6Al4V configuration, the average roughness in two materials in the design space is below 10 μm with a pressure of 250 MPa and below 6.5 μm with a pressure of 360 MPa. In the opposite configuration, the average roughness of the CFRP can reach 18 μm.

– In order to minimize the taper angle and the roughness, it is recommended to use high-pressure, low traverse feed rates. In addition, it is recommended to use the tool combination composed of an orifice of 0.25 mm, a focusing tube diameter of 0.76 and a mass flow rate of 350 g/min, in order to save water and abrasive resources and their associated costs. In addition, it is recommended to use the Ti6Al4V/CFRP configuration, since it may avoid the delamination of the CFRP material during piercing step, which should be analyzed in future works.

As a future line, the optimum parameters for the remaining piercing step should be also considered for avoiding the delamination on the final hole. In addition, it is recommended to study the effect of employing circular tool path over the obtained hole quality, and to study different strategies for starting and finishing the circular path.

Appendix

Table 5 Values of the process and physical parameters

Test	$d_s/d_e/\dot{m}_a$ [mm-mm-g/min]	Config. [−]	v [mm/min]	P [MPa]	$\pi1$ [MPa kg/s]	$\pi2_{Ti}$ [%]	$\pi2_{CFRP}$ [%]	$\pi3$ [kg]
1	0.25/0.76/350	Ti/CFRP	5	360	0.051	0	0.833	3.192
2	0.25/0.76/350	Ti/CFRP	5	250	0.035	0	1.235	3.192
3	0.25/0.76/350	Ti/CFRP	20	360	0.051	0	3.332	0.798
4	0.25/0.76/350	Ti/CFRP	20	250	0.035	0	4.938	0.798
5	0.25/0.76/350	Ti/CFRP	35	360	0.051	0	5.821	0.456
6	0.25/0.76/350	Ti/CFRP	35	250	0.035	0	8.628	0.456
7	0.25/0.76/350	Ti/CFRP	50	360	0.051	0	8.329	0.3192
8	0.25/0.76/350	Ti/CFRP	50	250	0.035	0	12.346	0.3192
9	0.25/0.76/350	Ti/CFRP	65	360	0.051	0	10.809	0.246
10	0.25/0.76/350	Ti/CFRP	65	250	0.035	0	16.022	0.246
11	0.25/0.76/350	Ti/CFRP	80	360	0.051	0	13.303	0.200
12	0.25/0.76/350	Ti/CFRP	80	250	0.035	0	19.719	0.200
13	0.25/0.76/350	Ti/CFRP	95	360	0.051	0	15.800	0.168
14	0.25/0.76/350	Ti/CFRP	95	250	0.035	0	23.416	0.168
15	0.25/0.76/350	CFRP/Ti	5	360	0.051	0.259	0	3.192
16	0.25/0.76/350	CFRP/Ti	5	250	0.035	0.384	0	3.192
17	0.25/0.76/350	CFRP/Ti	20	360	0.051	1.027	0	0.798
18	0.25/0.76/350	CFRP/Ti	20	250	0.035	1.523	0	0.798
19	0.25/0.76/350	CFRP/Ti	35	360	0.051	1.800	0	0.456
20	0.25/0.76/350	CFRP/Ti	35	250	0.035	2.668	0	0.456
21	0.25/0.76/350	CFRP/Ti	50	360	0.051	2.573	0	0.3192
22	0.25/0.76/350	CFRP/Ti	50	250	0.035	3.813	0	0.3192
23	0.25/0.76/350	CFRP/Ti	65	360	0.051	3.346	0	0.246
24	0.25/0.76/350	CFRP/Ti	65	250	0.035	4.959	0	0.246
25	0.25/0.76/350	CFRP/Ti	80	360	0.051	4.118	0	0.200
26	0.25/0.76/350	CFRP/Ti	80	250	0.035	6.104	0	0.200
27	0.25/0.76/350	CFRP/Ti	95	360	0.051	4.886	0	0.168
28	0.25/0.76/350	CFRP/Ti	95	250	0.035	7.243	0	0.168
29	0.35/1.02/450	Ti/CFRP	5	360	0.091	0	0.629	5.508
30	0.35/1.02/450	Ti/CFRP	5	250	0.063	0	0.911	5.508
31	0.35/1.02/450	Ti/CFRP	20	360	0.091	0	2.510	1.377
32	0.35/1.02/450	Ti/CFRP	20	250	0.063	0	3.634	1.377
33	0.35/1.02/450	Ti/CFRP	35	360	0.091	0	4.394	0.787
34	0.35/1.02/450	Ti/CFRP	35	250	0.063	0	6.362	0.787
35	0.35/1.02/450	Ti/CFRP	50	360	0.091	0	6.275	0.551
36	0.35/1.02/450	Ti/CFRP	50	250	0.063	0	9.085	0.551
37	0.35/1.02/450	Ti/CFRP	65	360	0.091	0	8.160	0.424
38	0.35/1.02/450	Ti/CFRP	65	250	0.063	0	11.813	0.424
39	0.35/1.02/450	Ti/CFRP	80	360	0.091	0	10.041	0.344
40	0.35/1.02/450	Ti/CFRP	80	250	0.063	0	14.536	0.344
41	0.35/1.02/450	Ti/CFRP	95	360	0.091	0	11.925	0.290
42	0.35/1.02/450	Ti/CFRP	95	250	0.063	0	17.264	0.290
43	0.35/1.02/450	CFRP/Ti	5	360	0.091	0.194	0	5.508
44	0.35/1.02/450	CFRP/Ti	5	250	0.063	0.281	0	5.508
45	0.35/1.02/450	CFRP/Ti	20	360	0.091	0.777	0	1.377

Table 5 (continued)

Test	$d_s/d_e/\dot{m}_a$ [mm-mm-g/min]	Config. [−]	v [mm/min]	P [MPa]	$\pi1$ [MPa kg/s]	$\pi2_{Ti}$ [%]	$\pi2_{CFRP}$ [%]	$\pi3$ [kg]
46	0.35/1.02/450	CFRP/Ti	20	250	0.063	1.125	0	1.377
47	0.35/1.02/450	CFRP/Ti	35	360	0.091	1.360	0	0.787
48	0.35/1.02/450	CFRP/Ti	35	250	0.063	1.969	0	0.787
49	0.35/1.02/450	CFRP/Ti	50	360	0.091	1.943	0	0.551
50	0.35/1.02/450	CFRP/Ti	50	250	0.063	2.813	0	0.551
51	0.35/1.02/450	CFRP/Ti	65	360	0.091	2.519	0	0.424
52	0.35/1.02/450	CFRP/Ti	65	250	0.063	3.647	0	0.424
53	0.35/1.02/450	CFRP/Ti	80	360	0.091	3.108	0	0.344
54	0.35/1.02/450	CFRP/Ti	80	250	0.063	4.500	0	0.344
55	0.35/1.02/450	CFRP/Ti	95	360	0.091	3.689	0	0.290
56	0.35/1.02/450	CFRP/Ti	95	250	0.063	5.339	0	0.290

References

1. Liu DF, Tang YJ, Cong WL (2012) A review of mechanical drilling of composite laminates. Compos Struct 94:1265–1279
2. Park KH, Beal A, Kim D, Kwon P, Lantrip J (2011) Tool wear in drilling composite/Ti6Al4V stacks using carbide and polycrystalline diamond tools. Wear 271:2826–2835
3. Poutord A, Rossi F, Poulachon G, M'Saoubi R, Abrivard G (2013) Local approach of wear in drilling Ti6Al4V/CFRP for stack modelling. Procedia CIRP 8:316–321
4. SenthilKumar M, Prabukarthi A, Krishnaraj V (2013) Study on tool wear and chip formation during drilling carbon fiber reinforced polymer (CFRP)/ Ti6Al4V Alloy (Ti6Al4V) stacks. Procedia Eng 64:582–592
5. Abrao AM, Faria PE, Campos Rubio JC, Reis P, Paulo Davim J (2007) Drilling of fiber reinforced plastics: a review. J Mater Process Technol 186:1–7
6. Shetty PK, Shetty R, Shetty D, Rehanan NF, Jose TK (2014) Machinability study on dry drilling of titanium alloy Ti-6Al-4V using L9 orthoganal array. Procedia Mater Sci 5:2605–2614
7. Chen SL, Yan BH, Huang FY (1999) Influence of kerosene and distilled water as dielectrics on the electric discharge machining characteristics of Ti-6Al-4V. J Mater Process Technol 87:107–111
8. Banyo Padhyay S, Sarin S, Sundararajan JK, Joshi G (2002) Geometrical features and metallurgic characteristics of Nd.YAG laser drilled holes in thick IN718 and Ti-6Al-4V sheets. J Mater Process Technol 127:83–95
9. Escobar-Palafox G, Wika K, Gault RS, Ridgway K (2012) Characterisation of abrasive water-jet process for drilling CFRP-Ti6Al4V stack. 21st International Conference on Waterjetting, 19–21 Sept, Ottowa, Canada
10. Ibraheem HMA, Iqbal A, Hashemipour M (2015) Numerical optimization of hole making in GFRP composite using abrasive water jet machining. J Chin Inst Eng 38:66–76
11. R. Pahuja, M. Ramulu, M. Hashish (2014) Abrasive Water jet machining (AWJ) of Hybrid Titanium/Graphite composite laminate (TiGr): Preliminary results. Proceedings of 22nd International Conference on Water Jetting, 3–5 Sept, Haarlem, Netherlands
12. Seo YW, Ramulu M, Kim D (2003) Machinability of Titanium Alloy (Ti6Al4V) by abrasive waterjets. Proc Inst Mech Eng B J Eng Manuf 217:1709–1721
13. Arola D, Ramulu M (1996) A study of kerf characteristics in abrasive waterjet machining of graphite/epoxy composite. ASME J Eng Mater Technol 118:256–265
14. Ramulu M, Arola D (1994) The influence of abrasive waterjet cutting conditions on the surface quality of graphite/epoxy laminates. Int J Mach Tools Manuf 34:295–313
15. Arola D, Ramulu M (1997) Material removal in abrasive waterjet machining of metals, surface integrity and texture. Wear 210:50–58
16. Alberdi A, Suárez A, Artaza T, Escobar-Palafox GA, Ridgway K (2013) Composite cutting with abrasive waterjet. Procedia Eng 63:421–429
17. Ramulu M, Arola D (1993) Waterjet and abrasive waterjet cutting of unidirectional graphite epoxy. Composites 24:299–308
18. Boud F, Carpenter C, Folkes J, Shipway PH (2010) Abrasive waterjet cutting of a Ti6Al4V alloy: the influence of abrasive morphology and mechanical properties on workpiece grit embedment and cut quality. J Mater Process Tecnhol 210:2197–2205
19. Hascalik A, Caydas U, Gürün H (2007) Effect of traverse speed on abrasive waterjet machining of Ti-6Al-4V alloy. Mater Des 28:1953–1957
20. Shanmugam DK, Nguyen T, Wang J (2008) A study of delamination on graphite/epoxy composites in abrasive waterjet machining. Compos Part A 39:923–929
21. Shanmugam DK, Wang J, Liu H (2008) Minimisation of kerf tapers in abrasive waterjet machining of alumina ceramics using a compensation technique. Int J Mach Tools Manuf 48:1527–1534
22. Shanmugam DK, Masood SH (2009) An investigation on kerf characteristics in abrasive waterjet cutting of layered composites. J Mater Process Technol 209:3887–3893
23. Wang J, Liu H (2006) Profile cutting on alumina ceramics by abrasive waterjet. Part 2: cutting performance models. Proc Inst Mech Eng C J Mech Eng Sci 220:715–725
24. Wang J (2007) Predictive depth of jet penetration models for abrasive waterjet cutting of alumina ceramics. Int J Mech Sci 49:306–316

25. Wang J (2009) A new model for predicting the depth of cut in abrasive waterjet contouring of alumina ceramics. J Mater Process Technol 209:2314–2320

26. Chen WL, Geskin ES (1990) Measurements of the velocity of abrasive waterjet by the use of laser transit anemometer. Proceedings of the 10th International Symposium on Jet Cutting Technolog, Amsterdam, Netherlands, pp 23–36

27. Hashish M (2005) Precision cutting of thick materials with AWJ. Proceedings of 17th International Conference on Waterjetting, Mainz, Germany, pp 33–45

28. Alberdi A, Rivero A, Lopez de Lacalle LN, Etxeberria I, Suarez A (2010) Effect of process parameters on the kerf geometry in abrasive waterjet milling. Int J Adv Manuf Technol 51:467–480

29. Zeng J (2007) Determination of machinability and abrasive cutting properties in AWJ cutting. Proceedings of the 2007 American Waterjet WJTA Conference, Houston, USA: paper 3-B